Optical characterization of niobium-doped rhenium disulphide single crystals

D. O. Dumcenco and Y. S. Huang[a)]
Department of Electronic Engineering, National Taiwan University of Science and Technology, Taipei 106, Taiwan

C. H. Liang and K. K. Tiong
Department of Electrical Engineering, National Taiwan Ocean University, Keelung 202, Taiwan

(Received 30 May 2007; accepted 24 August 2007; published online 19 October 2007)

In this study, the optical properties of niobium-doped rhenium disulphide (ReS_2:Nb) single crystals have been reported. The doping effects of the material were characterized by polarization-dependent transmittance, photoluminescence (PL), and piezoreflectance (PzR) measurements in the temperature range of 10–300 K. The indirect energy gap of ReS_2:Nb shows a slight redshift with respect to the undoped sample. The low temperature PL spectra reveal two near direct band-edge excitonic peaks as well as two additional prominent features at higher energy side. The results agree well with that of the PzR investigation of the sample. In comparison with the undoped ReS_2, the excitonic transition energies remain practically unchanged, while the broadening parameter of the excitonic transition features slightly increases due to impurity scattering. In addition, the parameters that describe the temperature variations of the band-edge excitonic transitions were evaluated and discussed. © *2007 American Institute of Physics*. [DOI: 10.1063/1.2798923]

I. INTRODUCTION

Rhenium disulfide is a semiconductor which belongs to VII-group layer-type structure family of the transition-metal dichalcogenides (TMDC) with a d^3 electron configuration.[1] Unlike most of other groups of layer TMDC crystals, ReS_2 crystallized in distorted $CdCl_2$ structure leading to triclinic symmetry.[2] ReS_2 crystallizes in a lattice with strong covalent bonds within a layer consisting of S–Re–S sheets and weak van der Waals interactions between the individual layers. Metal atoms in each ReS_2 crystal layer are actually displaced from the center of octahedral coordination units and formed the short metal-metal distances resulting in chains of metal atoms running through the structure along one of the in-plane axes.

Layered ReS_2 semiconductor is of considerable interest for various applications due to its optical, electrical, and mechanical properties.[3–5] These applications include a sulfur-tolerant hydrogenation and hydrodesulphurization catalyst,[6,7] and a promising solar-cell material in the electrochemical cells.[8–11] For the past decade, indirect semiconductors ReS_2 and $ReSe_2$ have also been attractive because of their highly anisotropic optical and electrical properties in the van der Waals plane.[12–16] The experimental results clearly indicated that near band-edge transitions (i.e., indirect band gap and excitons) in ReS_2 are polarization dependent.[17–20] The absorption-edge anisotropy in the layer plane of ReS_2 crystal possesses the potential capability to fabricate a polarization sensitive photodetector applied in multichannel optical communication for detecting the various orientations of linearly polarized light.[21,22] The polarization-dependent properties of indirect band gaps of ReS_2 observed by transmission measurements at room temperature provide a potential capability of this layer material to be used as an optical switch applied in polarized optical communication of near infrared (NIR) region.[19] A few works concerning the doping effect on the properties of ReS_2 and $ReSe_2$ compounds were reported.[23–25] Previous works indicate that doping leads to a redshift of the indirect energy gap while the direct band-edge excitonic transition energies remain practically unchanged.[12,24]

In this paper, we report the polarization-dependent optical properties study of ReS_2:Nb single crystals in the temperature range between 10 and 300 K. The indirect band-edge transitions were studied by means of polarization-dependent transmittance. The polarization-dependent photoluminescence (PL) and piezoreflectance (PzR) measurements were used for the determination of the direct band-edge excitonic transitions. The dominant excitonic lines of the PL spectrum were compared with the well-defined energies in the spectral range near the direct fundamental band gaps identified previously by PzR measurements. The doping effects of the material such as the redshift of the indirect energy gap and slight increases of broadening parameters of band-edge excitonic transitions are presented and discussed. The parameters that describe the temperature variations of the excitonic transitions in ReS_2:Nb layer crystals were evaluated and discussed.

II. EXPERIMENT

The niobium-doped rhenium disulfide single crystals were grown directly from the composite elements (Re: 99.99% pure, S: 99.999%, and Nb: 99.99%) by the vapor transport method using bromine as a transport agent.[26] The weight of doping material was determined stoichiometrically to obtain the nominal concentration ~1% of Nb. Total charge used in growth experiment was about 10 *g*. ReS_2:Nb

[a)]Author to whom correspondence should be addressed. Electronic mail: ysh@mail.ntust.edu.tw

single crystals, such as previously reported undoped ReS_2, formed thin silver-colored, graphitelike platelets up to 50 mm^2 (10×5 mm^2) in area and ~100 μm in thickness. Hall measurements indicate that the samples are *n* type in nature.

Single crystals with a thickness of about 10 μm were used for the transmittance measurements. Plate-shaped crystals were selected and mounted on a copper sample holder. A 150 W tungsten-halogen lamp filtered by a Photon Technology Inc. 0.25 m monochromator provided the monochromatic light. Measurements of the reflectivity and transmission at near-normal incidence configuration with a chopped light were carried out. Rochon prisms were employed for the polarization-dependent measurements. The PL measurements were carried out by collecting the light from the laser-illuminated face of the sample in a direction normal to the basal plane (001). The luminescence excitation was a double frequency YAG:Nd laser (YAG denotes yttrium aluminum garnet) (532 nm). The luminescence signals were analyzed by using a Jobin-Yvon "TRIAX 550" spectrometer equipped with a "SIMPHONY" charge coupled device (CCD) camera. In order to study the polarization properties of PL spectra, an analyzer placed just in front of the entrance slit of the spectrometer was used to set the direction of polarization vector **E** of the emission light.

The PzR measurements were achieved by gluing the thin single crystal specimens on a 0.15 cm thick lead-zirconate-titanate (PZT) piezoelectric transducer driven by a $200V_{rms}$ sinusoidal wave at 200 Hz.[27,28] The alternating expansion and contraction of the transducer subjects the sample to an alternating strain with a typical rms $\Delta l/l$ value of $\sim10^{-5}$. The reflected light was detected by EG&G type HUV-2000B silicon photodiode. The dc output of the silicon photodiode was maintained constant by a servo mechanism of a variable neutral density filter. A dual-phase lock-in amplifier was used to measure the detected signal. Modulated spectra were normalized to the reflectance to obtain $\Delta R/R$. An RMC model 22 close-cycle cryogenic refrigerator equipped with a digital thermometer controller was used to control the measurement temperature between 10 and 300 K with a temperature stability of 0.5 K or better.

III. RESULTS AND DISCUSSION

The crystal morphology and the crystal structure in the van der Waals plane of ReS_2:Nb are shown in Fig. 1. The weak van der Waals bonding between the layers of the material means a good cleavage property in the basal plane, which can be utilized to obtain thin specimen. The main crystal edges in the basal plane of ReS_2 correspond to the shortest and second shortest axes. The direction of the shortest axis can be determined by the layer splitting along as-grown thin dark lines which correspond to the longest crystal edge oriented along the Re-cluster chains. According to the structural parameters of ReS_2 crystals calculated previously from the spectra of x-ray diffraction, the in-plane **b** axis is parallel to the Re-cluster chains oriented along the [010] direction (see Fig. 1) and is always the shortest axis in the basal plane.[14] The measurements were performed for both $\mathbf{E}\|\mathbf{b}$ and $\mathbf{E}\perp\mathbf{b}$ polarizations.

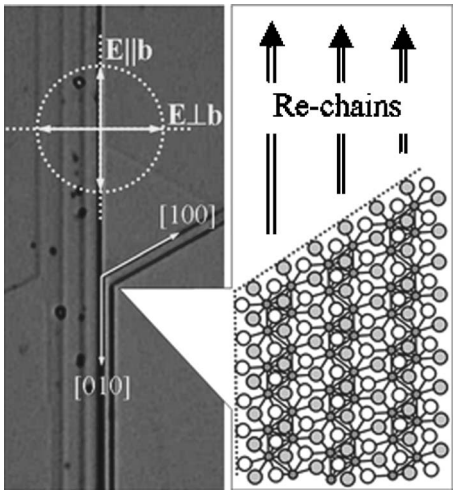

FIG. 1. The crystal morphology and crystal structure in the van der Waals plane of a Nb-doped ReS_2 single crystal.

The indirect band-edge transitions of the ReS_2:Nb were studied by means of polarization-dependent transmittance measured at near-normal incidence. The absorption coefficient α was determined from polarization-dependent optical transmittance by taking into account the spectral dependence of the reflectance using the relation[29]

$$T_r = \frac{(1-R)^2\exp(-\alpha d)}{1-R^2\exp(-2\alpha d)}, \tag{1}$$

where T_r represents the transmission coefficient, R is the reflectivity, and d is the sample thickness. The variation of the absorption coefficient of ReS_2:Nb with photon energy at several representative temperatures between 10 and 300 K is presented in Fig. 2. The open-square curve corresponds to the $\mathbf{E}\|\mathbf{b}$ polarization and the solid-square curve represents $\mathbf{E}\perp\mathbf{b}$ polarization for ReS_2:Nb. The small oscillations below the absorption edge attributed to interference effects are frequently observed for thin layered crystals.[30] The polarization dependence of the absorption curves provides conclusive evidence that the two optical absorption edges are associated with interband transitions from different origins. The polarization-dependent experimental data analysis of the absorption coefficient α shows an indirect allowed transition for the investigated materials.

The experimental points for $(\alpha h\nu)^{1/2}$ versus photon energy $h\nu$ deduced from polarization-dependent absorption measurements for ReS_2:Nb at several representative temperatures between 10 and 300 K are shown in Fig. 3. The open and solid squares are data points from the $\mathbf{E}\|\mathbf{b}$ and $\mathbf{E}\perp\mathbf{b}$ polarization measurements, respectively; and the solid curves are the least-squares fits to the expression[29]

$$\alpha h\nu = \frac{A(h\nu - E_g^{\mathrm{ind}} + E_p)^2}{\exp(E_p/kT)-1} + \frac{B(h\nu - E_g^{\mathrm{ind}} - E_p)^2}{1-\exp(-E_p/kT)}, \tag{2}$$

where $h\nu$ is the energy of the incident photon, E_g^{ind} is the indirect band gap, E_p is the energy of the phonon assisting

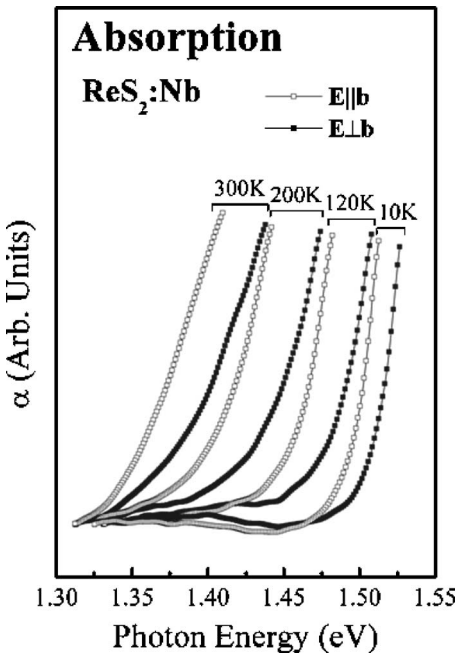

FIG. 2. Polarization-dependent absorption coefficient vs photon energy for ReS_2:Nb at several representative temperatures between 10 and 300 K. The open- and solid-square curves are deduced from the transmittance spectra of $\mathbf{E}\|\mathbf{b}$ and $\mathbf{E}\perp\mathbf{b}$ polarizations, respectively.

the transitions, and A and B are constants. The first term on the right-hand side of Eq. (2) corresponds to absorption of a photon and a phonon, whereas the second term corresponds to absorption of a photon and emission of a phonon and contributes only when $h\nu \geq E_g^{\mathrm{ind}} + E_p$. To evaluate the band gap E_g^{ind} and phonon energy E_p with the use of Eq. (2), the background absorption is subtracted out. The results indicate

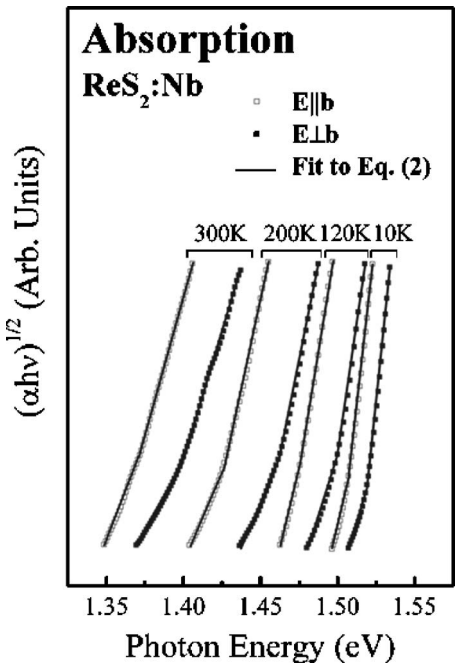

FIG. 3. Experimental points for $(\alpha h\nu)^{1/2}$ vs $h\nu$ that are deduced from polarization-dependent absorption measurements for ReS_2:Nb at several representative temperatures between 10 and 300 K. The open- and solid-squares are data points from the $\mathbf{E}\|\mathbf{b}$ and $\mathbf{E}\perp\mathbf{b}$ polarization measurements, respectively, and the solid curves are the least-squares fits to Eq. (2).

TABLE I. The summary of the indirect band gap energies and phonon energies obtained by polarization-dependent transmittance measurements for ReS_2:Nb, ReS_2:Mo, and undoped ReS_2.

Materials	Polarization	Energy gap E_g^{ind} (eV)	Phonon energy E_p (meV)
ReS_2:Nb[a]	$\mathbf{E}\|\mathbf{b}$	1.32±0.02	32±5
	$\mathbf{E}\perp\mathbf{b}$	1.35±0.02	27±5
ReS_2:Mo[b]	$\mathbf{E}\|\mathbf{b}$	1.31±0.02	32±5
	$\mathbf{E}\perp\mathbf{b}$	1.33±0.02	23±5
ReS[2c]	$\mathbf{E}\|\mathbf{b}$	1.35±0.02	25±5
	$\mathbf{E}\perp\mathbf{b}$	1.38±0.02	25±5

[a]This work.
[b]Reference 23.
[c]Reference 17.

that the Nb-doped sample is an indirect semiconductor, in which polarization along the Re chains exhibits a smaller band gap and a single phonon makes an important contribution in assisting the indirect transitions. The nonuniform thickness and nonsmooth sample surface will tend to cause the angles of incidence to deviate from the normal direction, resulting in some variations in the absorption spectra. The indirect gaps denoted as $E_{g\|}^{\mathrm{ind}}$ and $E_{g\perp}^{\mathrm{ind}}$ refer, respectively, to the indirect gap with $\mathbf{E}\|\mathbf{b}$ and $\mathbf{E}\perp\mathbf{b}$ polarizations. Differing values of E_g^{ind} and E_p could be obtained by fitting a different energy range; thus, errors of the order of ±0.02 eV and ±5 meV can be deduced for the estimates of E_g^{ind} and E_p, respectively. The fitted values of the energy gaps and phonon energy of the ReS_2:Nb crystals at room temperature are summarized in Table I. The results show that incorporation of small amounts of niobium into ReS_2 shifts the absorption edge by about 0.03 eV towards the lower energy region. This observation agreed well with the previous absorption study of Mo-doped ReS_2 single crystals.[23] The physical origin of the shift may come from the existence of n-type impurity, which in general will contribute to the absorption near the band tail. The parameters that describe the temperature dependence of the absorption edges with different polarizations in the van der Waals plane will be discussed in a latter section.

The typical unpolarized and polarization-dependent PL spectra of ReS_2:Nb in the 1.5–1.75 eV energy range at a constant laser excitation intensity of ~3 W/cm^2 (λ =532 nm) are illustrated in Fig. 4. Unpolarized PL spectra and the spectra with polarization perpendicular and parallel to the chains are shown by open-triangle, open-square, and open-circle curves, respectively. To assign simple radiative bands from the complex spectrum of photoluminescence, a multipeak Lorentzian line shape analysis offered by the software ORIGIN was employed. From the line shape fit, two well-resolved excitonic features marked by E_1^{ex} and E_2^{ex} at 1.552 and 1.585 eV with full width at half maximum (FWHM) of ~13.8 and ~14.6 meV, respectively, were observed in the PL spectra at 10 K. In addition, on the higher energy side of the spectra, another two peaks labeled as E_3^{ex} and E_4^{ex} appeared at energies of 1.631 and 1.645 eV, respectively. The two features located at the high energy side are

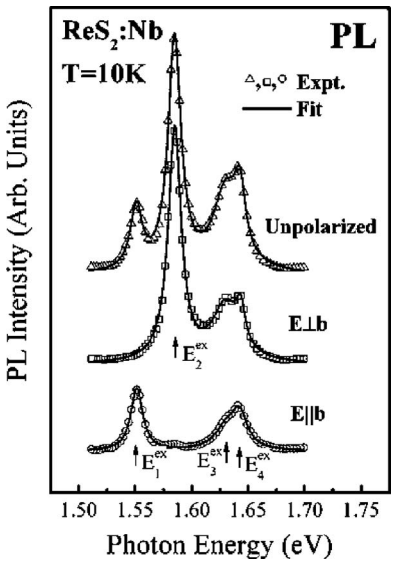

FIG. 4. The polarization-dependent PL spectra of ReS_2:Nb at 10 K. The figure shows the unpolarized (open triangles), and polarized perpendicular (open squares) and along (open circles) to **b**-axis PL spectra.

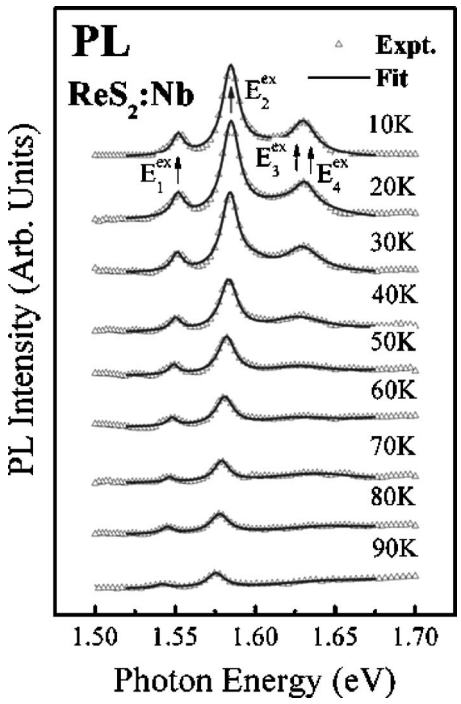

FIG. 5. Temperature-dependent unpolarized PL spectra of ReS_2:Nb in the temperature range between 10 and 90 K. The open triangles are the experimental data and the solid curves are the least-squares fits.

barely resolved with an energy separation of ~14 meV, while the well-resolved features E_1^{ex} and E_2^{ex} have an energy difference of ~33 meV. As shown in Fig. 4, the E_1^{ex} excitonic peak is forbidden for $\mathbf{E}\perp\mathbf{b}$ polarization, whereas the E_2^{ex} peak is disallowed for $\mathbf{E}\|\mathbf{b}$ polarization. Our experiments indicated that the two PL peaks E_3^{ex} and E_4^{ex} have shown no polarization dependency as both features were observed in $\mathbf{E}\|\mathbf{b}$ and $\mathbf{E}\perp\mathbf{b}$ polarization spectra. It is also worth noting that the intensities of E_3^{ex} and E_4^{ex} for the Nb-doped sample are significantly enhanced by comparing with the undoped and Mo-doped ReS_2. The entirely different polarization selection rules for these four features show that they originated from totally different origins. Temperature-dependent PL spectra of the excitonic transitions in the temperature range between 10 and 90 K are demonstrated in Fig. 5. The open triangles are the experimental data of unpolarized PL spectra and the solid lines are least-square fits to the multipeak Lorentzian line shape that yield transition energies indicated by arrows. As the temperature increases, the excitonic features demonstrate an energy redshift behavior as well as the decreasing character of line intensities. The intensities of E_3^{ex} and E_4^{ex} features decrease rather drastically with respect to temperature increasing and become completely quenched at $T=90$ K.

Previous research reports concerning the optical property study of ReS_2 utilizing PzR have revealed optical anisotropy consisting of strong polarization dependence of interband excitonic transitions in the vicinity of the direct band gap E_g^d.[12,31] The temperature-dependent PzR spectra of ReS_2:Nb with $\mathbf{E}\|\mathbf{b}$ and $\mathbf{E}\perp\mathbf{b}$ polarizations at various temperatures between 10 and 300 K are shown in Fig. 6. The open-circle and open-square curves are, respectively, the experimental PzR spectra of $\mathbf{E}\|\mathbf{b}$ and $\mathbf{E}\perp\mathbf{b}$ polarizations. In the low energy side of PzR spectra, two dominant structures associated with band-edge excitonic transitions were identified: the E_1^{ex} feature was detected at $\mathbf{E}\|\mathbf{b}$ polarization while E_2^{ex} feature was observed at $\mathbf{E}\perp\mathbf{b}$ polarization only.[12,17] The higher lying E_3^{ex} and E_4^{ex} features were also detected. It should be mentioned that intensity of PzR signal at the higher energy region is quite similar to the PL counterparts, showing considerable enhancement for Nb-doped ReS_2 in comparing with the previous investigations of undoped and Mo-doped ReS_2 single crystals.[12]

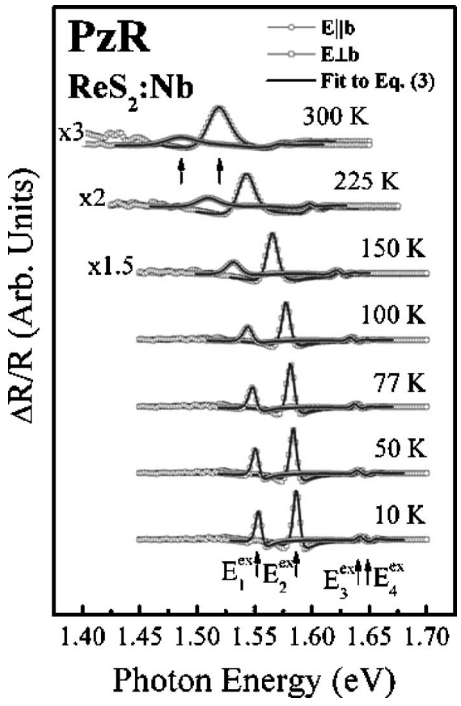

FIG. 6. Temperature-dependent PzR spectra of ReS_2:Nb at several temperatures between 10 and 300 K. The open circles and open squares correspond to the experimental data of $\mathbf{E}\|\mathbf{b}$ and $\mathbf{E}\perp\mathbf{b}$ polarizations, respectively, and the solid curves are least-squares fits to Eq. (3).

TABLE II. The summary of the energy positions and broadening parameters of the near band-edge excitonic transitions determined by polarization-dependent PzR measurements for ReS_2:Nb. Previous results of ReS_2:Mo and undoped ReS_2 are listed for comparison.

Material	Temperature (K)	Excitonic transition energy (eV)		Broadening parameter (meV)	
		E_1^{ex}	E_2^{ex}	Γ_1^{ex}	Γ_2^{ex}
ReS_2:Nb[a]	20	1.555±0.001	1.588±0.001	7±1	7±1
	300	1.485±0.002	1.519±0.002	32±2	22±2
ReS_2:Mo[b]	30	1.554±0.001	1.585±0.001	8±1	7±1
	300	1.485±0.002	1.516±0.002	35±2	23±2
ReS_2[b]	30	1.554±0.001	1.584±0.001	6±1	6±1
	300	1.484±0.002	1.518±0.002	31±2	21±2

[a]This work.
[b]Reference 23.

In order to determine the energy positions associated with observed optical transitions and to identify those unknown spectral features, the PzR spectrum of excitonic transitions has been fitted by a Lorentzian line shape expression,[32]

$$\frac{\Delta R}{R} = \mathrm{Re}\left[\sum_{i=1}^{n} A_i^{ex} e^{j\varphi_i^{ex}} (E - E_i^{ex} + j\Gamma_i^{ex})^{-2}\right], \quad (3)$$

where A_i^{ex} and φ_i^{ex} are the amplitude and phase of the line shape, and E_i^{ex} and Γ_i^{ex} are the energy and broadening parameters of the interband excitonic transitions, respectively. The fitting results illustrated as solid lines (Fig. 6) are the least-squares fits to the experimental data. Arrows at the bottom of PzR spectra show the peak positions of the main excitonic features, respectively. The values of transition energies and broadening parameters at room temperature and 10 K, analyzed by Eq. (3), are presented in Table II. The parameters of the near band-edge excitonic transitions determined by polarization-dependent PzR measurements of Mo-doped ReS_2 (Ref. 23) and undoped ReS_2 (Ref. 23) are listed in Table II for comparison purpose. The fitting results of ReS_2:Nb samples confirm that the direct band-edge excitonic transition energies E_1^{ex} and E_2^{ex} are not sensitive to a small concentration of niobium doping, and broadening parameter values are slightly increased due to impurity scattering. These observations agree with the results reported previously for Mo- and W-doped $ReSe_2$ single crystals.[24] The values of transition energies obtained in the PzR spectra are consistent with those of the PL spectra.

The experimental values of the temperature dependence of $E_1^{ex}(T)$ and $E_2^{ex}(T)$ as well as $E_{g\|}^{ind}(T)$ and $E_{g\perp}^{ind}(T)$ for ReS_2:Nb are presented in Fig. 7. The uncertainties of experimental data are expressed in the form of representative error bars. The dotted curves in Fig. 7 are the least-squares fit to the Varshni empirical relationship,[33]

$$E_i(T) = E_i(0) - \frac{\alpha_i T^2}{(\beta_i + T)}, \quad (4)$$

where $i=1$ or 2, $E_i(0)$ is the transition energy at 0 K, and α_i and β_i are Varshni coefficients. The constant α_i is related to the electron (exciton)-phonon interaction and β_i is closely related to the Debye temperature. The values of $E_i(0)$, α_i, and β_i obtained for excitonic transitions in ReS_2:Nb are listed in Table III. For comparison purposes, the numbers for undoped ReS_2 determined from PzR,[12] thermoreflectance (TR),[20] and photorefelctance[22] (PR) are also listed in Table III.

The temperature-dependent data of the interband excitonic transition energies have also been fitted by an expression containing the Bose-Einstein occupation factor for phonon,[34,35]

$$E_i(T) = E_{iB} - a_{iB}\left\{1 + \frac{2}{[\exp(\Theta_{iB}/T) - 1]}\right\}, \quad (5)$$

where $i=1$ or 2, a_{iB} represents the strength of the electron (exciton)-phonon interaction, and Θ_{iB} corresponds to the average phonon temperature. The fitted results are shown in Fig. 7 by solid lines. The obtained values of E_{iB}, a_{iB}, and Θ_{iB} for ReS_2:Nb, and the corresponding values for undoped ReS_2 determined from PzR (Ref. 12) and TR (Ref. 20) are given in Table III for comparison.

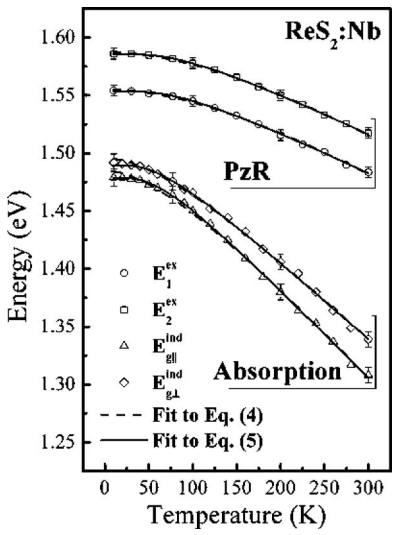

FIG. 7. The temperature dependence of the polarization-dependent excitonic transition energies and indirect band gaps of ReS_2:Nb with representative error bars. The dashed curves are the least-squares fits to Eq. (4) and the solid lines are fitted to Eq. (5).

TABLE III. The values of the fitting parameters of Varshni equation and an expression containing the Bose-Einstein occupation factor for phonon which describe the temperature dependence of polarization-dependent band-edge excitonic transition energies, and indirect band gaps determined from absorption (Abs) measurements of ReS_2:Nb and undoped ReS_2. The results obtained by TR and PR are also included for comparison.

Materials	Feature	$E(0)$ (eV)	α (meV/K)	β (K)	E_B (eV)	a_B (meV)	Θ_B (K)
ReS_2:Nb (PzR)[a]	E_1^{ex}	1.556±0.005	0.40±0.05	195±70	1.588±0.005	33±10	200±50
	E_2^{ex}	1.589±0.005	0.39±0.05	195±70	1.619±0.005	32±10	200±50
ReS_2 (PzR)[b]	E_1^{ex}	1.554±0.005	0.36±0.05	175±75	1.583±0.008	32±10	200±50
	E_2^{ex}	1.588±0.005	0.37±0.05	175±75	1.619±0.008	34±10	200±50
ReS_2 (TR)[c]	E_1^{ex}	1.546±0.001	0.34±0.05	180±70	1.584±0.002	37±15	240±60
	E_2^{ex}	1.577±0.001	0.33±0.05	190±70	1.613±0.002	35±14	240±60
ReS_2 (PR)[d]	E_1^{ex}	1.558±0.005	0.37±0.05	175±75			
	E_2^{ex}	1.591±0.005	0.35±0.05	180±75			
ReS_2:Nb (Abs)[a]	$E_{g\parallel}^{ind}$	1.48±0.02	0.86±0.05	130±50	1.55±0.02	70±20	180±50
	$E_{g\perp}^{ind}$	1.50±0.02	0.75±0.05	130±50	1.55±0.02	60±20	180±50
ReS_2 (Abs)[e]	$E_{g\parallel}^{ind}$	1.51±0.02	0.73±0.05	133±50	1.57±0.02	66±21	194±50
	$E_{g\perp}^{ind}$	1.52±0.02	0.68±0.05	128±50	1.58±0.02	62±18	193±50

[a]This work.
[b]Reference 12.
[c]Reference 20.
[d]Reference 22.
[e]Reference 15.

As shown in Table III, the values of the electron-phonon coupling constants α_i in Eq. (4) and a_{iB} in Eq. (5), which describe the temperature dependence of the indirect band gaps for ReS_2, are larger than those for the direct band-edge excitonic transition energies. The phenomena can be explained by the fact that the reduction in the thermal broadening of the exciton causes a faster shift of the absorption tail with temperature lowering. These results are similar to the previous reports on low energy absorption in MoS_2 and $MoSe_2$ layered crystals.[36]

The experimental values of the linewidth $\Gamma_i^{ex}(T)$ of ReS_2:Nb as obtained from the line shape fit are displayed in Fig. 8 by the solid open circles and open squares with representative error bars for the E_1^{ex} and E_2^{ex} excitonic transitions, respectively. The temperature dependence of the linewidth can be expressed as[34,35]

$$\Gamma_i(T) = \Gamma_{i0} + \frac{\Gamma_{iLO}}{[\exp(\Theta_{iLO}/T) - 1]}, \tag{6}$$

where $i=1$ or 2. The first term represents the broadening invoked from temperature-independent mechanisms, such as impurity, dislocation, electron interaction, and Auger processes, while the second term is caused by the Fröhlich interaction. The quantity Γ_{iLO} represents the strength of the electron (exciton)-LO phonon coupling while Θ_{iLO} is the LO phonon temperature. The solid curves in Fig. 8 represent least-squares fits of the experimental data which enable the evaluation of Γ_{i0}, Γ_{iLO}, and Θ_{iLO} for the excitonic transitions of ReS_2:Nb. The obtained values of these quantities are listed in Table IV together with the numbers for undoped ReS_2 determined by PzR (Ref. 12) and TR measurements.[20]

For comparison purposes, the numbers for fitting parameters from previous reports on polarization-dependent transition energies determination of undoped ReS_2 single crystals, measured by PzR,[12] TR,[20] and PR,[22] are also included. As shown in Table III, the values of Varshni coefficients α_i and β_i, and at the same time parameters of expression containing Bose-Einstein occupation factor a_{iB} and Θ_{iB} determined by PzR measurements of ReS_2:Nb, are in good agreement with previous fitting results of undoped ReS_2.[12] The β_i values for both E_1^{ex} and E_2^{ex} excitonic transitions equal to 195±70 K for ReS_2:Nb are in reasonable agreement with Debye temperature estimated from the Lindemann's formula for undoped ReS_2.[12] The high-temperature limits of Eqs. (4) and (5) yield

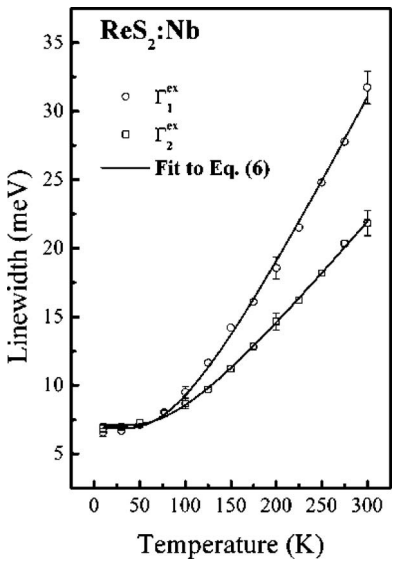

FIG. 8. The temperature dependence of the polarization-dependent linewidth of excitonic transitions of ReS_2:Nb with representative error bars. The solid curves are the least-squares fits to Eq. (6).

TABLE IV. The values of the parameters which describe the temperature dependence of the broadening function of the band-edge excitonic transitions of ReS_2:Nb and undoped ReS_2.

Materials	Feature	Γ_0 (meV)	Γ_{LO} (meV)	Θ_{LO} (K)
ReS_2:Nb[a]	E_1^{ex}	6.9±1.0	57±15	350±100
	E_2^{ex}	7.1±1.0	42±15	350±100
ReS_2 (PzR)[b]	E_1^{ex}	5.5±1.0	74±28	395±100
	E_2^{ex}	7.8±1.0	42±8	363±50
ReS_2 (TR)[c]	E_1^{ex}	9.5±0.5	36±15	326±100
	E_2^{ex}	8.0±0.5	30±17	348±100

[a]This work.
[b]Reference 12.
[c]Reference 20.

an expression $\alpha_i \approx 2a_{iB}/\Theta_{iB}$ which is satisfied within error bars for the obtained parameters α_i, a_{iB}, and Θ_{iB} of Table III. The temperature variations of excitonic-transition energies are due to both the lattice-constant variations and interactions with relevant acoustic and optical phonons. According to the existing theory, this should lead to a value of Θ_{iB} significantly smaller than Θ_{iLO} and agree favorably with our present experimental investigations.

The values of the parameters which describe the temperature dependence of broadening function of the excitonic transitions of ReS_2:Nb are comparable to those of undoped ReS_2. The values for the coupling constant Γ_{1LO} and Γ_{2LO} for ReS_2:Nb are in the range of 40–60 meV, which are considerably larger than those reported for a number of semiconductors, such as GaAs (~20 meV) (Ref. 37) and ZnSe (~24 meV).[38] We suspected that the large values of Γ_{LO} may be the general characteristics of crystals with layer structure. However, a more systematic experimentation should be carried out to verify this property.

IV. SUMMARY

The effects of Nb dopant on the optical properties were studied. The results indicate that incorporation of niobium into the host lattice ReS_2 can cause a small redshift of the indirect energy gap of the Nb-doped ReS_2 sample as determined from the transmittance spectra. The PL spectra of ReS_2:Nb observed by means of linearly polarized light at normal incidence to the basal plane revealed two strongly polarization-dependent main peaks, E_1^{ex} and E_2^{ex}, while the higher lying E_3^{ex} and E_4^{ex} peaks have shown no polarization dependence. The direct band-edge excitonic transition energies E_1^{ex} and E_2^{ex} of ReS_2:Nb single crystals obtained by PzR measurements remain practically unchanged in comparison with undoped ReS_2. Nevertheless, the doping effect shows up in a slight increase of the broadening parameter of the excitonic features. It is also worth noting that, by doping with niobium, the intensities of the higher lying E_3^{ex} and E_4^{ex} peaks have significantly enhanced over that of the samples doped with Mo.

ACKNOWLEDGMENT

The authors would like to acknowledge the financial support by the National Science Council of Taiwan under Grant Nos. NSC95-2112-M-011-001, NSC95-2221-E-011-171, and NSC 95-2112-M-019-001.

[1] J. A. Wilson, F. J. DiSalvo, and S. Mahajan, Adv. Phys. **24**, 117 (1975).
[2] J. C. Wildervanck and F. Jellinek, J. Less-Common Met. **24**, 73 (1971).
[3] J. A. Wilson and A. D. Yoffe, Adv. Phys. **18**, 193 (1969).
[4] G. Leicht, H. Berger, and F. Levy, Solid State Commun. **61**, 531 (1987).
[5] K. Friemelt, O. Kulikova, L. Kulyuk, A. Siminel, E. Arushanov, Ch. Kloc, and E. Bucher, J. Appl. Phys. **79**, 9268 (1996).
[6] H. S. Broadbent, L. H. Slaugh, and N. L. Jarvis, J. Am. Chem. Soc. **76**, 1519 (1954).
[7] S. Harris and R. R. Chianelli, J. Catal. **86**, 400 (1984).
[8] F. P. Koffyberg, K. Dwight, and A. Wold, Solid State Commun. **30**, 433 (1979).
[9] B. L. Wheeler, J. K. Leland, and A. J. Bard, J. Electrochem. Soc. **133**, 358 (1986).
[10] J. V. Marzik, R. Kershaw, K. Dwight, and A. Wold, J. Solid State Chem. **51**, 170 (1984).
[11] B. Schubert and H. Tributsch, J. Appl. Electrochem. **20**, 786 (1990).
[12] C. H. Ho, P. C. Liao, Y. S. Huang, and K. K. Tiong, Phys. Rev. B **55**, 15608 (1997).
[13] K. K. Tiong, C. H. Ho, and Y. S. Huang, Solid State Commun. **111**, 635 (1999).
[14] C. H. Ho, Y. S. Huang, P. C. Liao, and K. K. Tiong, J. Phys. Chem. Solids **60**, 1797 (1999).
[15] C. H. Ho, Y. S. Huang, K. K. Tiong, and P. C. Liao, Phys. Rev. B **58**, 16130 (1998).
[16] C. H. Ho, Y. S. Huang, J. L. Chen, T. E. Dann, and K. K. Tiong, Phys. Rev. B **60**, 15766 (1999).
[17] C. H. Ho, Y. S. Huang, K. K. Tiong, and P. C. Liao, J. Phys.: Condens. Matter **11**, 5367 (1999).
[18] C. H. Ho, P. C. Yen, Y. S. Huang, and K. K. Tiong, J. Phys.: Condens. Matter **13**, 8145 (2001).
[19] C. H. Ho, H. W. Lee, and C. C. Wu, J. Phys.: Condens. Matter **16**, 5937 (2004).
[20] C. H. Ho, Opt. Express **13**, 8 (2004).
[21] K. Friemelt, M.-Ch. Lux-Steiner, and E. Bucher, J. Appl. Phys. **74**, 5266 (1993).
[22] C. H. Ho, P. C. Yen, Y. S. Huang, and K. K. Tiong, Phys. Rev. B **66**, 245207 (2002).
[23] P. C. Yen, M. J. Chen, Y. S. Huang, C. H. Ho, and K. K. Tiong, J. Phys.: Condens. Matter **14**, 4737 (2002).
[24] S. Y. Hu, S. C. Lin, K. K. Tiong, P. C. Yen, Y. S. Huang, C. H. Ho, and P. C. Liao, J. Alloys Compd. **383**, 63 (2004).
[25] S. Y. Hu, C. H. Liang, K. K. Tiong, Y. S. Huang, and Y. C. Lee, J. Electrochem. Soc. **153**, J100 (2006).
[26] Y. S. Huang, Chin. J. Phys. (Taipei) **22**, 43 (1984).
[27] F. H. Pollak and H. Shen, Mater. Sci. Eng., R. **10**, 275 (1993).
[28] H. Mathieu, J. Allegre, and B. Gil, Phys. Rev. B **43**, 2218 (1991).
[29] J. I. Pankove, *Optical Processes in Semiconductors* (Dover, New York, 1975).
[30] K. K. Kam, C. L. Chang, and D. W. Lynch, J. Phys. C **17**, 4031 (1984).
[31] C. H. Ho, P. C. Liao, Y. S. Huang, and K. K. Tiong, Solid State Commun. **103**, 19 (1997).
[32] D. E. Aspnes, in *Handbook on Semiconductors*, edited by M. Balkanski (North-Holland, Amsterdam, 1980), p. 109.
[33] Y. P. Varshni, Physica (Amsterdam) **34**, 149 (1967).
[34] P. Lantenschlager, M. Garriga, S. Logothetidis, and M. Cardona, Phys. Rev. B **35**, 9174 (1987).
[35] P. Lantenschlager, M. Garriga, L. Vina, and M. Cardona, Phys. Rev. B **36**, 4821 (1987).
[36] A. M. Goldberg, A. R. Beal, F. A. Levy, and E. A. Davis, Philos. Mag. **32**, 367 (1975).
[37] H. Qiang, F. H. Pollak, C. M. Sotomayer Torres, W. Leitch, A. H. Kean, M. Stroscio, G. J. Jafrate, and K. W. Kim, Appl. Phys. Lett. **61**, 1411 (1992).
[38] L. Malikova, W. Krystek, F. H. Pollak, N. Dai, A. Cavus, and M. C. Tamargo, Phys. Rev. B **54**, 1819 (1996).

INSTITUTE OF PHYSICS PUBLISHING JOURNAL OF PHYSICS: CONDENSED MATTER

J. Phys.: Condens. Matter **15** (2003) 1487–1494 PII: S0953-8984(03)55681-8

The first-order Raman spectra of OsO_2

P C Yen[1], R S Chen[1], Y S Huang[1,4], C T Chia[2], R H Chen[2] and K K Tiong[3]

[1] Department of Electronic Engineering, National Taiwan University of Science and Technology, Taipei 106, Taiwan, Republic of China
[2] Department of Physics, National Taiwan Normal University, Taipei 117, Taiwan, Republic of China
[3] Department of Electrical Engineering, National Taiwan Ocean University, Keelung 202, Taiwan, Republic of China

Received 6 November 2002, in final form 22 January 2003
Published 24 February 2003
Online at stacks.iop.org/JPhysCM/15/1487

Abstract

The first-order Raman spectra of the transition metal dioxide OsO_2 with tetragonal rutile structure have been measured at room temperature. A linearly polarized argon laser light source and completely oriented single-crystal samples have made possible unambiguous determination of the four allowed Raman-active phonon modes. Comparison is made with results for other rutile materials.

1. Introduction

The family of transition metal dioxide compounds with rutile-type structure possesses an interesting variety of electrical and magnetic properties [1]. Conductive transition metal dioxides with rutile-type structure show potential applications in substituting for the metals currently used in conductive lines which serve to connect components of semiconductor and electrode materials in ferroelectric memory devices [2–4]. Osmium dioxide, OsO_2, belongs to this family of compounds; little is known of its fundamental properties. This may be due in part to the highly toxic nature of the readily formed and volatile tetroxide of the material [5].

This report presents the first-order Raman spectra of OsO_2. To the best of our knowledge only one such report on the phonon frequencies of the four Raman-active modes in OsO_2 exists [6]. The existing literature merely lists a Raman spectrum from a small crystal of OsO_2, oriented so as to display all four Raman-active lines. In the present study, the group symmetry restraints of the Raman-active phonons and the Raman selection rules are discussed. The results are then utilized to classify the experimentally observed polarized Raman spectra of the four phonon modes. Comparisons are made with results for other metal dioxide [7–13] and metal fluoride [10, 14] compounds, which possess similar rutile-type structure.

[4] Author to whom any correspondence should be addressed.

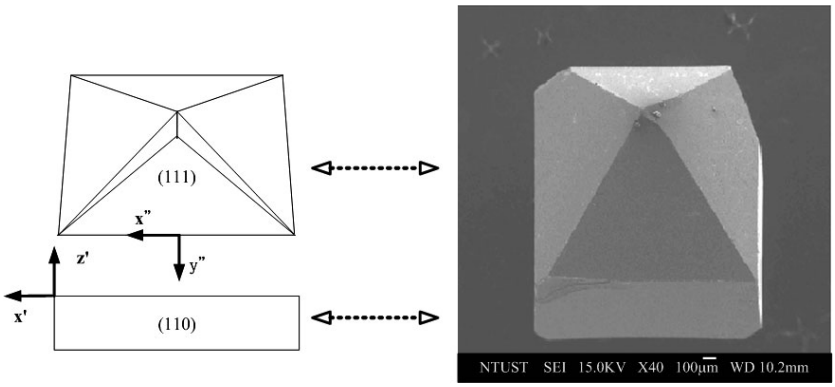

Figure 1. A photograph of an OsO_2 crystal showing the (110) and (111) planes together with the polarization axes.

2. Experimental details

Single crystals of OsO_2 with well-developed faces were grown in our laboratory by the chemical transport method [15]. OsO_2 was grown by the oxidation of high-purity osmium with excess $NaClO_3$ or $NaBrO_3$ in an evacuated, sealed silica tube. The volume of the tube was about 100 cm^3 after sealing, and the excess $NaClO_3$ or $NaBrO_3$ was sufficient to complete oxidation of Os to OsO_2. The processes of $NaClO_3$ or $NaBrO_3$ decomposition and Os oxidation were accomplished simultaneously by slowly heating the silica tube and its contents to 300 °C over 48 h and subsequently firing at 650 °C for an additional 48 h. This treatment resulted in an apparent complete decomposition of the chlorate or bromate with the formation of golden OsO_2 powder in one end of the tube. The tube was then transferred to a horizontal furnace and positioned so as to provide a temperature gradient along the length of the tube, which is about 20 cm long. The charge of OsO_2 in one end was maintained at 920 °C, and the opposite end of the tube was held at 900 °C for 240 h. The transported crystals were about 3–5 mm across a polyhedral face. The x-ray powder diffraction analysis was performed to ascertain that tetragonal rutile structure had been obtained. The crystals were x-ray pre-oriented with respect to the directions and polarizations of the incident and scattered light. A representative crystal showing the as-grown (110) and (111) planes together with the prescribed polarization configurations is illustrated in figure 1.

Raman measurements were made on as-grown (110) and (111) faces in the backscattering geometry utilizing a DILOR XY-800 triple-grating Raman spectrometer equipped with a liquid-nitrogen-cooled CCD and an OLYMPUS BH-2 microscope. The 5145 Å line of an argon ion laser was used as the excitation source, and was focused on the sample surface with a 100× objective. The focusing spot size is about 1 μm in diameter and the laser power density is estimated to be about 1 W cm^{-2}. Prior to the measurement, the system was calibrated by means of the 520 cm^{-1} Raman peak of a Si single crystal. The spectra exhibited approximately a 0.5 cm^{-1} resolution with the slit width of 30 μm. For frequency less than 250 cm^{-1}, an argon purge was used to suppress the N_2 lines.

3. Symmetry analysis

OsO_2 has the tetragonal rutile structure belonging to the space group D_{4h}^{14} with two OsO_2 molecules per unit cell as shown in figure 2. The cations are located at sites with D_{2h} symmetry

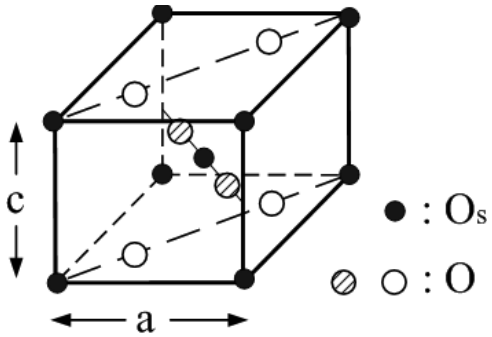

Figure 2. A schematic representation for a unit cell of OsO_2.

and the anions occupy sites with C_{2v} symmetry. The Os ions are surrounded by six oxygen ions at the corners of a slightly distorted octahedron, while the three Os ions coordinating each of the oxygen ions lie in a plane at the corners of a nearly equilateral triangle. There are four Raman-active modes with symmetries A_{1g}, B_{1g}, B_{2g}, and E_g [15]. The first three are singlets and the last is a doublet.

Corresponding to each Raman-active mode, there is a scattering tensor α having a distinctive symmetry. For the four allowed Raman transitions in materials of D_{4h}^{14} space group, these tensors have the form [16]

$$\alpha(A_{1g}) = \begin{pmatrix} a & 0 & 0 \\ 0 & a & 0 \\ 0 & 0 & b \end{pmatrix}, \qquad \alpha(B_{1g}) = \begin{pmatrix} c & 0 & 0 \\ 0 & -c & 0 \\ 0 & 0 & 0 \end{pmatrix}, \qquad \alpha(B_{2g}) = \begin{pmatrix} 0 & d & 0 \\ d & 0 & 0 \\ 0 & 0 & 0 \end{pmatrix}$$
$$\alpha(E_g) = \begin{pmatrix} 0 & 0 & 0 \\ 0 & 0 & e \\ 0 & e & 0 \end{pmatrix} \qquad \text{and} \qquad \begin{pmatrix} 0 & 0 & e \\ 0 & 0 & 0 \\ e & 0 & 0 \end{pmatrix}. \tag{1}$$

The displacements of atoms associated with the four Raman-active vibrations are shown in figure 3 [9]. To examine experimentally a given component α_{ij}, the geometry is arranged such that the incident light is polarized in the i-direction while only the scattered light of j-polarization is observed.

A full classification of the four Raman-active modes may be accomplished as follows. The geometric configurations for the various axes used in this experiment are denoted as

$$\begin{aligned} x' &= \frac{1}{\sqrt{2}}(1\bar{1}0) & x'' &= \frac{1}{\sqrt{2}}(1\bar{1}0) \\ y' &= \frac{1}{\sqrt{2}}(110) & y'' &= \frac{1}{\sqrt{6}}(11\bar{2}) \\ z' &= (001) & z'' &= \frac{1}{\sqrt{3}}(111). \end{aligned} \tag{2}$$

The expressions for the relative Raman intensities correlating to various $|\alpha_{ij}|^2$ for the two different crystal orientations along (110) and (111) faces in the backscattering configurations are listed in table 1. The results show that the B_{1g} mode is forbidden for all configurations for scattering from the (110) face and is allowed only for the $\alpha_{x''y''}$-configuration from the (111) face. The E_g mode is allowed for $\alpha_{x'z'}$-, $\alpha_{x''y''}$-, and $\alpha_{y''y''}$-configurations, while the allowed configurations for the A_{1g} mode are $\alpha_{x'x'}$, $\alpha_{z'z'}$, $\alpha_{x''x''}$, and $\alpha_{y''y''}$. The B_{2g} mode is allowed for $\alpha_{x'x'}$-, $\alpha_{x''x''}$-, and $\alpha_{y''y''}$-configurations.

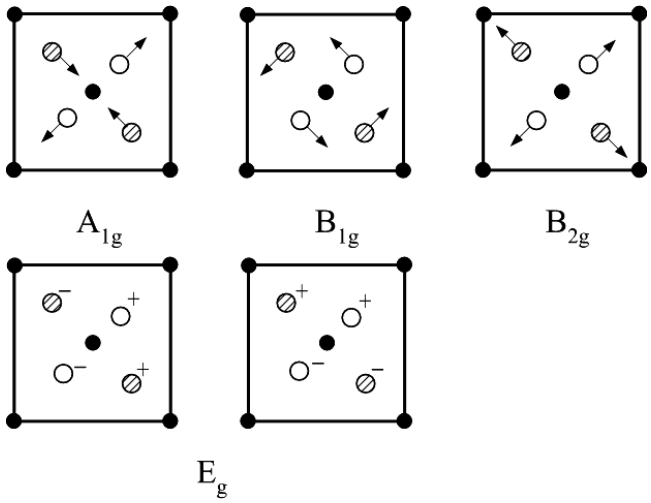

Figure 3. The displacements of atoms of OsO_2, viewed along the *c*-axis, associated with the four first-order Raman-active modes of rutile structure.

Table 1. Relative Raman intensities for the B_{1g}, E_g, A_{1g}, and B_{2g} phonon modes for the various polarization configurations used in this experiment.

	Phonon mode			
Polarization configuration	B_{1g}	E_g	A_{1g}	B_{2g}
			(110) face	
$\alpha_{x'x'}$	0	0	a^2	d^2
$\alpha_{x'z'}$	0	e^2	0	0
$\alpha_{z'z'}$	0	0	b^2	0
			(111) face	
$\alpha_{x''x''}$	0	0	a^2	d^2
$\alpha_{x''y''}$	$(1/3)c^2$	$(2/3)e^2$	0	0
$\alpha_{y''y''}$	0	$(8/9)e^2$	$(1/9)(a+2b)^2$	$(1/9)d^2$

4. Results and discussion

Plotted in figures 4(a)–(c) are the Raman spectra observed for scattering from the as-grown (110) surface of single-crystal OsO_2 for the cases of $\alpha_{x'x'}$-, $\alpha_{x'z'}$-, and $\alpha_{z'z'}$-configurations, respectively. Figure 4(a) shows two Raman peaks at 685 and 726 cm^{-1} whereas figures 4(b) and (c) show only one peak each at 544 and 685 cm^{-1}, respectively. Mode assignment with the aid of table 1 shows that these features correspond to the E_g mode (544 cm^{-1}), the A_{1g} mode (685 cm^{-1}), and the B_{2g} phonon (726 cm^{-1}). Our identification of the peak positions of the three lines agreed extremely well with that of [6], which is so far the only report on the material.

In figures 5(a)–(c) we display the Raman spectra seen for scattering from the (111) face for the polarization arrangements $\alpha_{x''x''}$, $\alpha_{x''y''}$, and $\alpha_{y''y''}$, respectively. Note that in figure 5(b), in addition to a strong peak at 544 cm^{-1}, a very sharp weak feature at 184 cm^{-1} is observed. This is the B_{1g} phonon mode and the peak position agrees very well with that of [6] where it is determined as being at 187 cm^{-1}. This is the only configuration where the B_{1g} line is

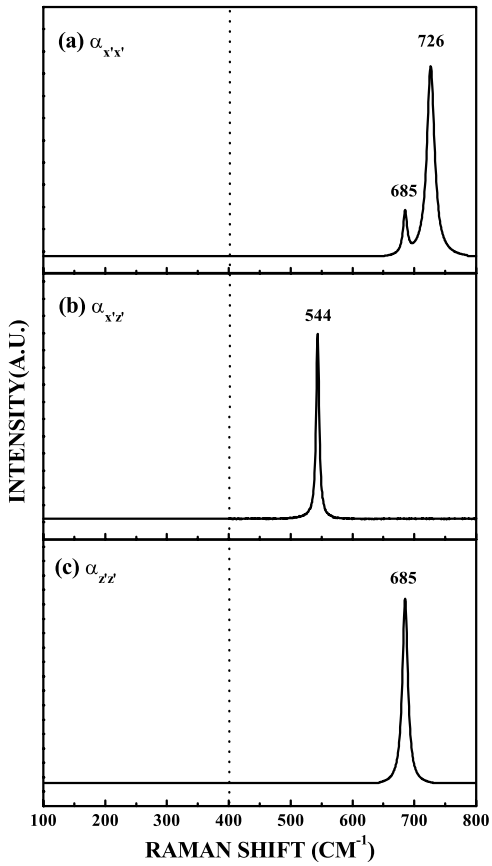

Figure 4. The Raman spectra observed for scattering from the (110) surface of single-crystal OsO_2. (a) The $\alpha_{x'x'}$-configuration showing the A_{1g} and B_{2g} phonons at 685 and 726 cm^{-1}, respectively. (b) The $\alpha_{x'z'}$-configuration showing the E_g phonon at 544 cm^{-1}. (c) The $\alpha_{z'z'}$-configuration showing the A_{1g} phonon at 685 cm^{-1}.

allowed (see table 1). The polarization configurations of the other three Raman signatures at locations 544, 685, and 726 cm^{-1} lead to a consistent symmetry assignment of these structures as indicated by table 1 and with that given by figures 4(a)–(c). It is also worth noting that the relative intensity ratios of B_{2g} to A_{1g} modes for $\alpha_{x'x'}$- and $\alpha_{x''x''}$-configurations are consistent with that given by table 1, where $I(B_{2g})/I(A_{1g}) = d^2/a^2 \approx 3.4$.

As shown in figures 4 and 5, the Raman spectra of OsO_2 exhibit strong lines of A_{1g}, E_g symmetries, a high-frequency line of B_{2g} symmetry, and a very sharp and weak low-frequency B_{1g} mode. A careful search for the B_{1g} mode is necessary, since the intensity of this mode is smaller than that of the E_g mode by a factor of 50 or more. The frequency and symmetry assignments for the four Raman-active phonons of OsO_2 are listed in table 2. For completeness and comparison, the table also summarizes the previously reported results for a number of other metal dioxides (OsO_2 [6], RuO_2 [7, 8], IrO_2 [9], TiO_2 [10], SnO_2 [11], and CrO_2 [12]), GeO_2 [13], and metal fluorides (MgF_2 [10], ZnF_2 [10], FeF_2 [10], MnF_2 [10], and CoF_2 [14]) with the rutile structure.

The Raman spectra of OsO_2 are quite sharp, with very little background. The observed full width at half-maximum (FWHM) at room temperature is about 2.4, 6.2, 8.3, and 14.4 cm^{-1}

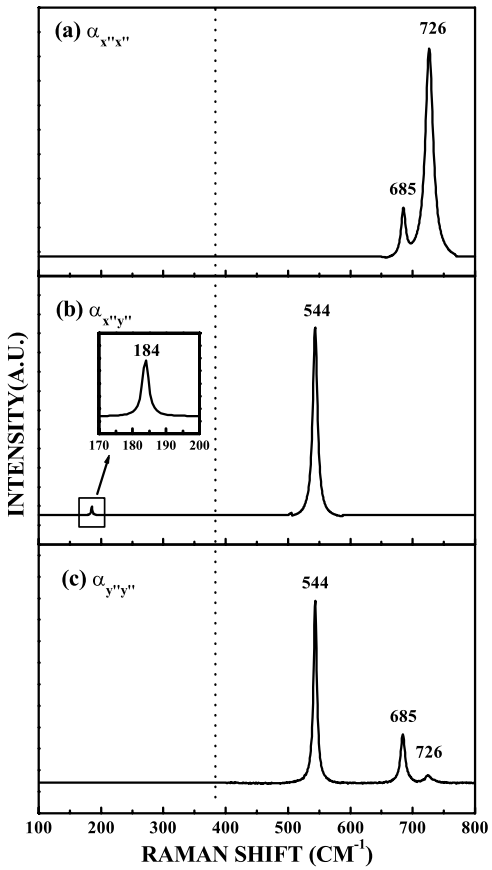

Figure 5. The Raman spectra observed for scattering from the (111) surface of single-crystal OsO_2. (a) The $\alpha_{x''x''}$-configuration showing the A_{1g} and B_{2g} phonons at 685 and 726 cm^{-1}, respectively. (b) The $\alpha_{x''y''}$-configuration showing the B_{1g} and E_g phonons at 184 and 544 cm^{-1}, respectively. (c) The $\alpha_{y''y''}$-configuration showing the E_g, A_{1g}, and B_{2g} phonons at 544, 685, and 726 cm^{-1}, respectively.

for B_{1g}, A_{1g}, E_g, and B_{2g} modes, respectively. These values are comparable to those for the insulating rutile materials and unlike those for metallic VO_2 [18] (rutile structure), for which only a strong, broad band near 550 cm^{-1} has been observed. It is also most appropriate to compare the Raman spectra of OsO_2 to those of the isostructural dioxide compounds of Ir, Ru, and Cr. The B_{2g} mode of these metal dioxides is comparatively soft as compared to the corresponding phonon modes of the insulating metal oxides TiO_2 [10] and SnO_2 [11]. The relative intensities of the B_{2g} mode in the metallic materials OsO_2 (see figures 4 and 5), IrO_2, RuO_2, and CrO_2 are considerably greater compared to those for the transparent rutile materials [9, 10, 12]. Srivastava and Chase [12] have attributed this behaviour in CrO_2 to a plasma-edge-induced resonance enhancement. In the B_{2g} mode, all of the nearest-neighbour oxygen atoms move toward one cation and away from the other inequivalent cation in the unit cell. This mode is likely to be resonance enhanced by the plasma edge present in the metallic-like oxides because of the charge density fluctuations produced near the cation sites by such oxygen displacements. Table 2 shows that OsO_2 has the hardest B_{1g} mode of all the rutile materials investigated to date. The similarity of the Raman-active phonons for OsO_2 and

Table 2. Raman-active phonons in a number of materials with the rutile structure.

	Mode (cm^{-1})			
Material	B_{1g}	E_g	A_{1g}	B_{2g}
OsO_2[a]	184	544	685	726
OsO_2 [6]	187	545	685	727
RuO_2 [7]	97	528	646	716
RuO_2 [8]	165	526	646	715
IrO_2 [9]	145	561	752	728
TiO_2 [10]	143	447	612	826
SnO_2 [11]	123	475	634	776
CrO_2 [12]	—	470	575	700
GeO_2 [13]	97	680	702	870
MgF_2 [10]	92	295	410	515
ZnF_2 [10]	70	253	350	522
FeF_2 [10]	73	257	340	496
MnF_2 [10]	61	247	341	476
CoF_2[b] [14]	68	246	366	494

[a] Present work.
[b] Measured at 77 K.

RuO_2 is quite striking—except for the value for the soft B_{1g} mode from [7]. The two reports, references [7] and [8], on RuO_2 differed significantly only as regards the location of the soft B_{1g} mode (97 cm^{-1} for [7] and 165 cm^{-1} for [8]). It is speculated that such a discrepancy may result from slight oxygen deficiency [8] (and references within) in the samples used in [7]. In any case, the higher frequency value of 165 cm^{-1} seems to be more consistent with the values for B_{1g} modes for the other metal dioxides with rutile structure [9–11] and most significantly with the value of 184 cm^{-1} (187 cm^{-1} from [6]) for OsO_2. The reason for the close similarity is that OsO_2 and RuO_2 are structurally identical, with four d electrons per cation. The relatively weak oscillator strength for the B_{1g} mode, as shown consistently by our results and the previous reports [6–9], indicates an inherent physical character for rutile structure crystals belonging to the D_{4h}^{14} space group.

5. Summary

In summary, the polarized first-order Raman spectra have been measured at room temperature for single crystals of metallic OsO_2. The four Raman-active phonons predicted by group theory have been observed and classified. Comparison is made with results for other rutile materials. The B_{2g} mode is softer compared to the corresponding phonons in the insulating material oxides, while OsO_2 shows the hardest B_{1g} mode of all the rutile materials investigated to date.

Acknowledgment

The authors acknowledge the support of the National Science Council of the Republic of China.

References

[1] Mattheiss L F 1976 *Phys. Rev.* B **13** 2433
[2] Kolawa E, So F C T, Pan E T S and Nicolet M A 1987 *Appl. Phys. Lett.* **50** 854

[3] Nakamura T, Nakao Y, Kamisawa A and Takasu H 1994 *Appl. Phys. Lett.* **65** 1522
[4] Al-Shareef H N, Bellur K R, Kingon A I and Auciell O 1995 *Appl. Phys. Lett.* **66** 239
[5] Balfour W J and Ram R S 1984 *J. Mol. Spectrosc.* **105** 360
[6] Weber W H and Merlin R 2000 *Raman Scattering in Materials Science* (Berlin: Springer)
[7] Huang Y S and Pollak F H 1982 *Solid State Commun.* **43** 921
[8] Rosenblum S S, Weber W H and Chamberland B L 1997 *Phys. Rev.* B **56** 529
[9] Huang Y S, Lin S S, Huang C R, Lee M C, Dann T E and Chien F Z 1989 *Solid State Commun.* **70** 517
[10] Porto S P S, Fleury P A and Damen T C 1967 *Phys. Rev.* **154** 522
[11] Peercy P S and Morosin B 1973 *Phys. Rev.* B **7** 2779
[12] Srivastava R and Chase L L 1972 *Solid State Commun.* **11** 349
[13] Scott J F 1970 *Phys. Rev.* B **1** 3488
[14] MacFarlane R M and Ushioda S 1970 *Solid State Commun.* **8** 1081
[15] Schäfer H 1964 *Chemical Transport Reactions* (New York: Academic)
[16] Loudon R 1964 *Adv. Phys.* **13** 423
[17] Loudon R 1963 *Proc. Phys. Soc.* **82** 393
[18] Srivastava R and Chase L L 1971 *Phys. Rev. Lett.* **27** 727